Numerical and experimental evidence of the inter-blade cavitation vortex development at deep part load operation of a Francis turbine

K Yamamoto[1], A Müller[1], A Favrel[1], C Landry[1] and F Avellan[1]

[1]EPFL-LMH, Avenue de Cour 33bis, 1007 Lausanne, Switzerland

keita.yamamoto@epfl.ch

Abstract. Francis turbines are subject to various types of the cavitation flow depending on the operating conditions. In order to compensate for the stochastic nature of renewable energy sources, it is more and more required to extend the operating range of the generating units, from deep part load to full load conditions. In the deep part load condition, the formation of cavitation vortices in the turbine blade to blade channels called inter-blade cavitation vortex is often observed. The understanding of the dynamic characteristics of these inter-blade vortices and their formation mechanisms is of key importance in an effort of developing reliable flow simulation tools. This paper reports the numerical and experimental investigations carried out in order to establish the vortex characteristics, especially the inception and the development of the vortex structure. The unsteady RANS simulation for the multiphase flow is performed with the SST-SAS turbulence model by using the commercial flow solver ANSYS CFX. The simulation results in terms of the vortex structure and the cavitation volume are evaluated by comparing them to the flow visualizations of the blade channel acquired through a specially instrumented guide vane as well as from the downstream of the runner across the draft tube cone. The inter-blade cavitation vortex is successfully captured by the simulation and both numerical and experimental results evidence that the inter-blade vortices are attached to the runner hub.

1. Introduction

Hydraulic turbines are often subject to cavitation flow, and various types of cavitation are observed depending on the discharge and head conditions [1, 2]. In particular, the cavitation vortex rope developing in the draft tube cone at the runner outlet can occasionally generate instabilities and prevent the stable operation of the generating unit [3]. Therefore, a large number of researches including one-dimensional stability analyses, a hydro-acoustic resonance analysis, a study of the locally induced discharge fluctuations and cavitation vortex dynamics, as well as measurements of the velocity field surrounding the cavitation vortex rope have been performed and reported [4, 5, 6, 7]. Recently, in order to mitigate the stochastic nature of variable renewable energy sources, hydraulic turbines are more and more required to enhance their flexibility by extending the operating range down to the deep part load operating condition. However, the characteristics of the cavitation phenomena observed in the deep part load operating condition, especially inter-blade cavitation vortices, are not fully understood yet due to the limited number of the researches about the deep part load operation in the past [8, 9].

In a first step of the experimental approach, the inter-blade vortices are visualized from the low pressure side of the turbine across the transparent diffuser cone with an inclined window [10]. In addition to that, a novel technique to visualize the blade channel from the high pressure side of the turbine by using an

instrumented guide vane with a transparent window and appropriate lighting is developed. First visualizations of inter-blade cavitation vortices from this new perspective are reported in [11]. In the numerical approach, it is found that the computation of the inter-blade vortex is quite sensitive to the mesh grid size in the turbine blade channel. [12]

In the present study, the inter-blade cavitation vortex captured by the visualization techniques described in [10] and [11] are compared to the results of the unsteady RANS simulation performed by ANSYS CFX, and then the flow structures inside the turbine blade channel are investigated. Moreover, the development of the inter-blade vortex development are briefly explained by the correlation of the static pressure, flow velocity, vorticity and streamline at each plane of the constant span.

2. Setups

2.1. Experimental setup

The experiments are carried out with a 1:16 reduced scale model of a Francis turbine of $\nu = 0.27$ with 8 piezo-resistive pressure sensors installed in the draft tube cone at two different streamwise positions. Furthermore the pressure at the runner inlet is monitored with 4 equally spaced sensors in the head cover, located on the same radius as the guide vane axes. The torque acting on the shaft, the mean discharge, the turbine rotational frequency and turbine specific energy are also monitored and recorded simultaneously throughout all the measurements. The mean discharge is adjusted by the guide vane opening angle, and the turbine specific energy is controlled by the rotational frequency of two axial double-volute pumps. The pressure level in the draft tube is set by a vacuum pump in the downstream reservoir.

Both visualizations from the high and low pressure sides of the turbine are carried out in order to investigate the inter-blade cavitation vortex features. The visualization from the high pressure side produces particularly suitable outcomes for the comparison with the numerical simulation results. For this visualization, instrumented guide vanes with a transparent acrylic window and a boroscope for the optical access to the blade channel are prepared. As a light source, a compact LED featuring 10 W and a Xenon flash light are adopted depending on the frame rate of the image acquisition. A sketch of the instrumented guide vane and the entire installation of the visualization equipment is shown in Figure 1. All the technical details and acquisition procedures are summarized in [11].

The experiments are carried out focusing on one operating condition at a guide vane opening angle $\alpha = 5\,\mathrm{degree}$. The specific values of the operating condition are summarized in Table 1.
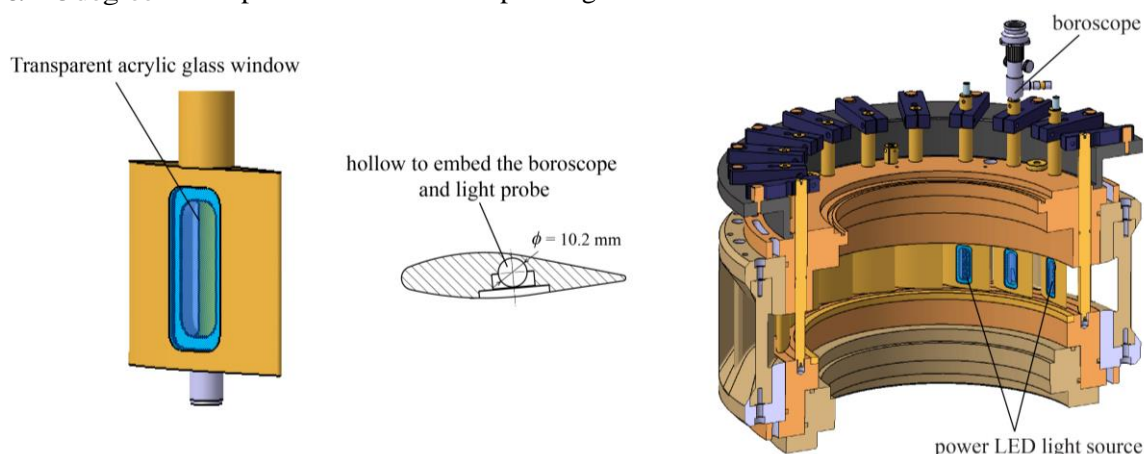

Figure 1. Experimental setup for the visualization of the inter-blade cavitation from the turbine inlet

Table 1 Operating condition for the measurements

OP	GV. Opening α	Rotating frequency n	Specific energy E	Q/Q_{BEP}	Thoma σ
DPL2	5	14.67 Hz	263 J kg^{-1}	27.0 %	0.11

2.2. Numerical simulation setup

The unsteady RANS simulation is carried out by using the commercial flow solver ANSYS CFX 15.0. In the performed simulation, a two phase flow is treated as a homogeneous fluid, hence, the phases are assumed to share a common flow field such as pressure and velocity. The equations of mass conservation and momentum conservation for the homogeneous mixture are written respectively;

$$\frac{\partial \rho}{\partial t} + \nabla \cdot \left(\rho \vec{C} \right) = 0 \tag{1}$$

$$\frac{\partial \rho \vec{C}}{\partial t} + \left(\rho \vec{C} \cdot \nabla \right) \vec{C} = -\nabla p + \nabla \cdot \left(\overline{\overline{\tau}} + \overline{\overline{\tau}}_t \right) \tag{2}$$

where ρ, C, p, $\overline{\overline{\tau}}$, and $\overline{\overline{\tau}}_t$ represent mixture density, mixture velocity, the mixture pressure, viscous stress tensor and turbulent stress tensor, respectively. The mixture density is expressed as follows by using the liquid volume fraction γ_l, the vapour volume fraction $\gamma_v = 1 - \gamma_l$, the liquid density ρ_l, and the vapour density ρ_v.

$$\rho = \rho_l \gamma_l + \rho_v \gamma_v = \rho_l \gamma_l + \rho_v (1 - \gamma_l) \tag{3}$$

Cavitation is taken into account by solving the transport equation. The transport equation for the vapour volume fraction is written as;

$$\frac{\partial \gamma_v}{\partial t} + \left(\vec{C} \cdot \nabla \right) \gamma_v = \frac{1}{\rho_v} \left(S_{vp} + S_{cn} \right) \tag{4}$$

where S_{vp} and S_{cn} represent the source term of the vaporization and condensation processes. These terms are derived from the simplified Rayleigh-Plesset equation describing the dynamics of the gas bubble in a liquid.

$$S_{vp} = F_{vp} \frac{3 \gamma_{nuc} \left(1 - \gamma_v \right) \rho_v}{R_B} \sqrt{\frac{2}{3} \frac{p_v - p}{\rho_l}}, \text{ if } p < p_v \tag{5}$$

$$S_{cn} = F_{cn} \frac{3 \gamma_{nuc} \gamma_v \rho_v}{R_B} \sqrt{\frac{2}{3} \frac{p - p_v}{\rho_l}}, \text{if } p > p_v \tag{6}$$

where γ_{nuc} and R_B are the volume fraction of the nucleation sites and the radius of a bubble, respectively. F_{vp} and F_{cn}, are empirical factors taking into account the fact that the vaporization and condensation processes have different time scales. In this study, the following default values of CFX are used [13]:

$$\gamma_{nuc} = 5 \times 10^{-4}, R_B = 10^{-6} \text{ (m)}, F_{vp} = 50, \text{ and } F_{cn} = 0.01 \tag{7}$$

For the unsteady RANS simulation, the turbulence model is of key importance for the accurate prediction of the flow field. For the presented simulation, SST-SAS (Scale Adaptive Simulation) model is adopted as a turbulence model. The governing equation of the SST-SAS model introduces the SAS source term based on the von Karman length scale in the transport equation for the turbulence eddy frequency, which allows the model to dynamically adjust to resolved structures in a URANS simulation [14]. The SAS-SST model provides results similar to LES particularly in the unsteady flow region, and this model is used for various industrial applications with satisfactory results in recent years [15, 16].

The computational domain includes the spiral case, stay vanes, guide vanes, runner, diffuser cone and draft tube with about 16 million nodes in total as shown in Figure 2, in particular, about 8.5 million nodes are distributed to the runner domain (see the right-hand side of Figure 2). As a boundary condition, bulk mass flow rate and static pressure extracted from the experimental result are imposed on the inlet and outlet, respectively. For the time step, 0.0001 s corresponding to about 0.5 degree of the runner revolution is selected.
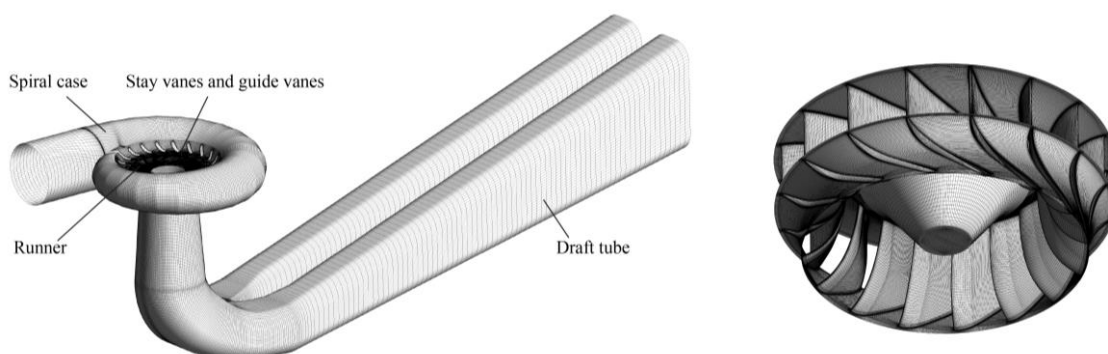
Figure 2. Computational domain of the unsteady RANS simulation

3. Results

The images of the inter-blade cavitation vortex acquired by the visualization from both sides of the turbine inlet and outlet as well as the result of the numerical simulation are shown in Figure 3. The surface of cavitation is defined by the 10 % void fraction. It can be confirmed that the simulated inter-blade cavitation vortex has a good agreement with the visualized inter-blade cavitation. Both results demonstrate that the inter-blade cavitation vortex is clearly attached on the hub, and the helical vortex filament is developed in the channel.
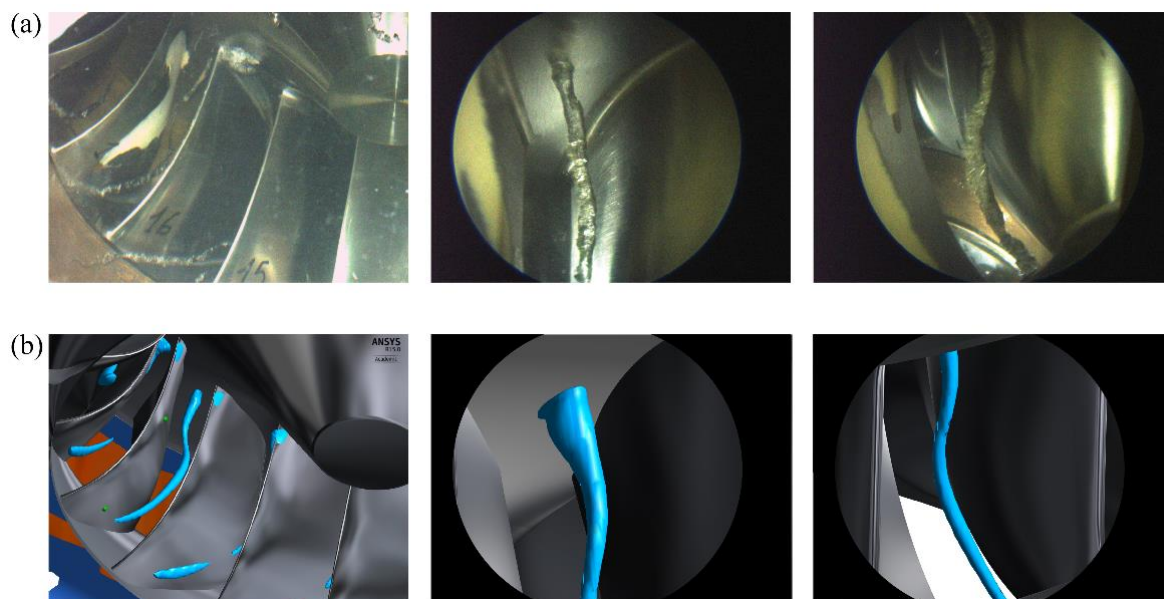
Figure 3. Comparison of the inter-blade cavitation vortex in the experiment (a) with the simulation (b)

In Figure 4, the entire view of the turbine with the iso-surface of the Q-criterion $1.0 \times 10^6 \, \text{s}^{-2}$ coloured by the level of the void fraction and the cavitation surface defined by the 10% void fraction is presented. According to the figure, the vortex structure highlighted by the Q-criterion iso-surface is clearly developed inside each blade channel, and cavitation is formed along this vortex structure. It can be also confirmed that the void fraction becomes particularly high near the runner hub, which evidences that the prospect of the cavitation occurrence is potentially high in this region. While the void fraction is low in the middle span, the high void fraction region appears again when the vortex approaches the runner outlet where the static pressure is relatively low. Accordingly, the cavitation is formed again around the outlet of the runner.
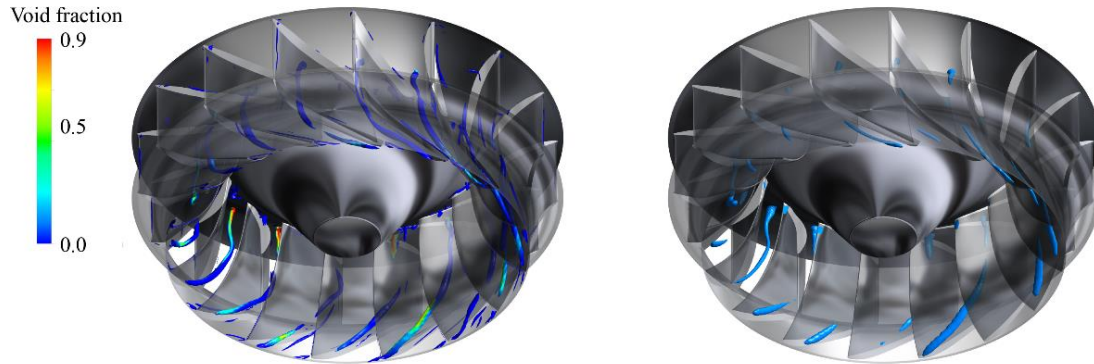
Figure 4. Iso-surface of the Q-criterion coloured by the void fraction and the cavitation surface defined by the void fraction 10 %

In Figure 5, the three components of the circumferentially averaged velocity (C_u, C_m and C_{span}) at the runner inlet and the meridional view of the circumferentially averaged meridional velocity C_m are shown. Referring to the meridional velocity component C_m which corresponds to the radial velocity at the runner inlet, the magnitude of the velocity C_m close to the runner hub and shroud becomes relatively higher than the velocity in the middle span region. It can be also confirmed in the meridional view of the meridional velocity in the right-hand side of Figure 5. The relatively high velocity region highlighted by the red colour appears close to the hub and shroud regions, whereas the flow around the hub close to the blade trailing edge is dominated by the separated flow region having almost no velocity.
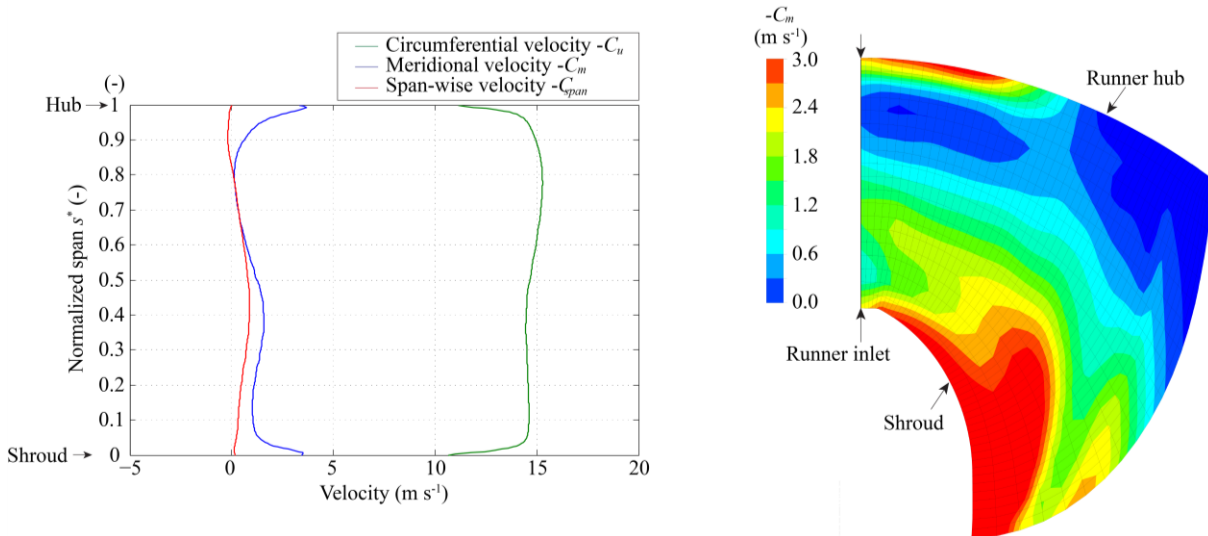

Figure 5. Velocity distribution at the turbine inlet and the meridional view of the circumferentially averaged meridional velocity
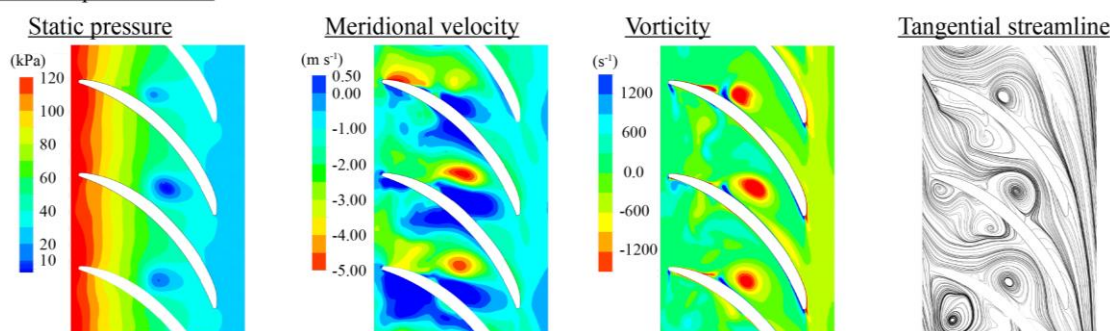
In Figure 6, the static pressure, the meridional velocity, the vorticity, and the tangential streamline at a constant normalized span-wise locations $s^* = 0.99$, 0.50, and 0.10 are shown, respectively. At normalized span plane $s^* = 0.99$, the velocity is particularly high at the inlet, on the other hand, the velocity is stalled in the separated flow region close to the runner outlet. The collision of the high velocity flow at the inlet with the stalled velocity region generates a strong vorticity as confirmed in the vorticity contour and the tangential streamline, hence, the low pressure zone is induced in the core of the vortex. In accordance with this low pressure region induced by the strong vorticity, the high void fraction appears particularly close to the hub. This vortex is then carried by the main flow in the blade channel, and develops the vortex filament in the blade channel. At the middle span $s^* = 0.50$, the vortex structure is still clearly observed although the stalled velocity region is almost diminished. At the

normalized span $s^* = 0.10$, the vortex structure approaches the runner outlet where the pressure is essentially lower than the pressure at the runner inlet, which results in a high void fraction again at the centre of the vortex. According to the contour of the meridional velocity and the tangential streamline, the flow is more uniformly distributed compared to the cases of $s^* = 0.99$ and 0.50, which evidences that the non-uniformity of the flow close to the runner hub plays a significant role on the inception of the inter-blade vortex.

(a) Normalized span $s^* = 0.99$
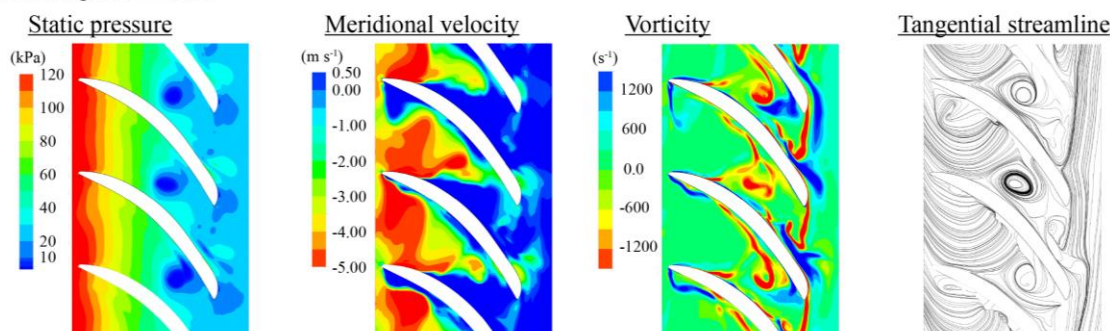
(b) Normalized span $s^* = 0.50$

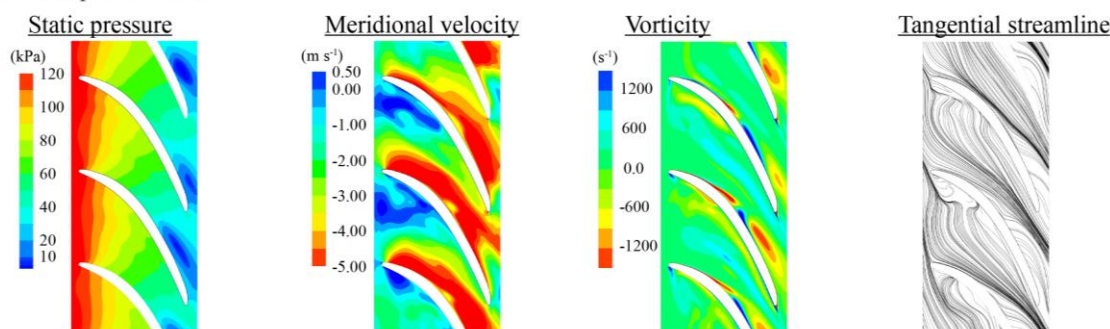
(c) Normalized span $s^* = 0.10$

Figure 6. Static pressure, meridional velocity, vorticity and tangential streamline at each constant normalized span $s^* = 0.99$ (a), $s^* = 0.50$ (b), and $s^* = 0.10$ (c)

4. Conclusions and perspectives

It is shown that the inter-blade cavitation vortex is well captured by the introduced visualization techniques using specially instrumented guide vanes. These visualization results are also used for the evaluation of the numerical simulation, and the comparison demonstrates that the inter-blade cavitation is successfully replicated by the unsteady RANS simulation performed with the SST-SAS turbulence model which enables the dynamic adjustment to the resolution of small turbulent structures. Both experimental and numerical results evidence that the inter-blade cavitation vortex is clearly attached to the runner hub. The numerical simulation furthermore suggests that a region with the strong vorticity is

created by the collision of the relatively high velocity and the separated flow region close to the hub. Correspondingly, the low pressure region appears in the centre of the vortex resulting in the formation of the inter-blade cavitation vortex.

The development of the inter-blade vortex will be more precisely investigated in the ongoing research, especially looking into the flow separation analysis using the skin friction lines on the runner hub wall. Furthermore, the unsteady characteristics of the inter-blade vortex is also surveyed by comparison of the simulated pressure on the runner blades with the pressure fluctuations measured on the blade through the telemetry measurement system of the experiments.

5. Acknowledgements

6. References

[1]   Avellan F. (2004). Introduction to Cavitation in Hydraulic Machinery, Proc. of the *6th International Conference on Hydraulic Machinery and Hydrodynamics*, Timisoara, Romania

[2]   Escaler X., Egusquiza E., Farhat M., Avellan F. and Coussirat M. (2006). Detection of cavitation in hydraulic turbines, *Journal of Mechanical Systems and Signal Processing*, Vol.20, Issue4, pp.983-1007

[3]   Rheingans W. J. (1940). Power Swings in Hydroelectric Power Plants, Transaction of ASME 62, pp. 171-184

[4]   Alligné S., Nicolet C., Tsujimoto Y, and Avellan F. (2014). Cavitation surge modelling in Francis turbine draft tube. *Journal of Hydraulic Research*, Vol. 52, pp. 399–411

[5]   Müller A., Yamamoto K., Alligné S., Yonezawa K., Tsujimoto Y., and Avellan F. (2016) Measurement of the Self-Oscillating Vortex Rope Dynamics for Hydroacoustic Stability Analysis, *Journal of Fluid Engineering*, Vol. 138, Issue 2, No. 21206

[6]   Müller A., Dreyer M., Andreini N., Avellan F. (2013). Draft tube discharge fluctuation during self-sustained pressure surge: Fluorescent particle image velocimetry in two-phase flow, *Experiments in Fluids*, Vol.54, Issue 4, pp.1-11

[7]   Favrel A., Landry C., Müller A. Yamamoto K., and Avellan F. (2015). Study of the vortex-induced pressure excitation source in a Francis turbine draft tube by particle image velocimetry, *Experiments in Fluids*, Vol.56, Issue 12, pp. 1-15

[8]   Farhat, M., Natal, S., Avellan, F., Paquet, F. and Couston, M. (2002). Onboard Measurements of pressure and strain Fluctuations in a Model of Low Head Francis Turbine – Part 1: Instruction, Proc. of the *21th IAHR Symposium on Hydraulic Machinery and Systems*, Lausanne, Switzerland

[9]   Lowys, P. Y., Paquet, F., Couston, M., Farhat, M., Natal, S. and Avellan, F. (2002). Onboard Measurements of pressure and strain Fluctuations in a Model of Low Head Francis Turbine – Part 2: Measurements and Preliminary Analysis Results, Proc. of the *21th IAHR Symposium on Hydraulic Machinery and Systems*, Lausanne, Switzerland

[10]   Yamamoto K., Müller A., Favrel A., Landry C., Avellan F. (2014). Pressure measurements and high speed visualizations of the cavitation phenomena at deep part load condition in a Francis turbine, *IOP Conference Series: Earth and Environmental Science*, Art. No. 22011

[11]   Yamamoto K., Müller A., Favrel A., Landry C., Avellan F. (2015). Guide vanes embedded visualization technique for investigating Francis runner inter-blade vortices at deep part load operation, Proc. of the *6th IAHR International Meeting of the Workgroup on Cavitation and Dynamic Problems in Hydraulic Machinery and Systems*, Ljubljana, Slovenia

[12] Wack J., and Riedelbauch S. (2015). Numerical simulations of the cavitation phenomena in a Francis turbine at deep part load conditions, *Journal of Physics: Conference Series*, Vol. 656, Art. No. 012074

[13] Zwart, P., Gerber, A. G., and Belamri, T. (2004). A two-phase model for predicting cavitation dynamics, *5th International Conference on Multiphase Flow,* Yokohama

[14] Menter F. R., and Egorov Y. (2010). Development and Application of SST-SAS Turbulence Model in the DESIDER Project, *Advances in Hybrid RANS-LES Modelling, Notes on Numerical Fluid Mechanics and Multidisciplinary* Design, Vol. 97, pp.113-138

[15] Menter F. R., and Egorov Y. (2010). The scale-adaptive simulation method for unsteady turbulent flow predictions. part 1: Theory and model description, *Flow, Turbulence and Combustion*, Vol. 85, pp.113-138

[16] Egorov Y., Menter F. R., Lechner R., and Cokljat D. (2010). The scale-adaptive simulation method for unsteady turbulent flow predictions. part 2: Application to complex flows, *Flow, Turbulence and Combustion*, Vol. 85, pp.139-165